Laser spectroscopic measurements of binding energies and fine-structure splittings of Co^-, Ni^-, Rh^-, and Pd^-

Michael Scheer, Cicely A. Brodie, René C. Bilodeau, and Harold K. Haugen*
Department of Physics and Astronomy, McMaster University, Hamilton, Ontario, Canada L8S 4M1
(Received 20 April 1998)

A tunable infrared laser source is utilized to study the photodetachment threshold spectra of the transition-metal negative ions Co^-, Ni^-, Rh^-, and Pd^-. The binding energies of the respective ionic ground states are found to be 663.3(6), 1157.16(12), 1142.89(20), and 562.14(12) meV. In addition, a $^3F_4-^3F_3$ fine-structure splitting of 875(15) cm^{-1} is measured for Co^-, and the $^2D_{5/2}-^2D_{3/2}$ splitting of Ni^- is determined to be 1485(3) cm^{-1}. For Pd^-, the electronically excited $4d^9 5s^2\ ^2D_{5/2}$ state is found to lie 1127(4) cm^{-1} above the $4d^{10}5s\ ^2S_{1/2}$ ionic ground state, i.e., it is bound by 422.4(5) meV. The results agree with previous values obtained from laser photodetached electron spectra, but constitute improvements in accuracy of up to two orders of magnitude. [S1050-2947(98)05009-4]

PACS number(s): 32.80.Gc, 32.10.Hq, 32.10.Fn

I. INTRODUCTION

Over the past three decades negative ions have attracted considerable attention from theorists as well as experimentalists due to both their fundamental and practical implications. More recent efforts have investigated various species and phenomena such as molecular ions [1], continuum resonances [2], metastable states [3], ions in strong fields [4], and resonant multiphoton detachment [5–7]. Progress in the knowledge of binding energies in atomic negative ions has continued since the 1985 review article by Hotop and Lineberger [8]. Still, the stable negative ion states of many elements remain only poorly known, and in some cases even totally unknown.

Most experimental determinations of negative ion binding energies are based on either laser photodetachment threshold (LPT) studies or laser photodetached electron spectrometry (LPES). LPES is a powerful technique, as it can be applied to virtually any stable negative ion, irrespective of the binding energy to be measured. The accuracy of measured energy values is, however, limited to the resolution of the electron spectrometer, which is typically a few meV. Accuracies of LPT measurements, on the other hand, range from 0.1 to 0.001 meV, as they are often only limited by the laser bandwidth. The constraint on LPT studies involving detachment to the atomic ground state is that the tunable photon energies have to match the ionic binding energies. Most previous LPT studies have utilized visible laser light and have therefore been restricted to systems with electron affinities (EA's) larger than 1.4 eV. (A notable exception are the alkali-metal and alkaline-earth negative ions, where detachment to excited states of the respective atoms and state selective detection schemes were employed [3,9].) In particular, of the 25 transition metals that are expected or known to form stable negative ions, only the strongly bound Ir^-, Pt^-, and Au^- ions have been previously investigated via LPT methods. The applicability of *infrared* LPT to the study of weakly bound negative ions (the EA is less than 1 eV) was first demonstrated by Feldmann [10]. This investigation of P^-, and our recent studies of B^- [11] and Al^- [12], have shown that infrared LPT spectroscopy can provide accurate electron affinities as well as ionic fine-structure splittings.

The fine structure of the initial ionic and the final atomic state is manifested in the photodetachment spectrum as a series of cascaded thresholds. For each of these thresholds, Wigner's threshold law for photodetachment [13] predicts a partial cross section proportional to $\varepsilon^{\ell+1/2}$, where ε is the energy of the detached electron and ℓ is its angular momentum. In the above cases of ions with valence p electrons, the detached electron carries no angular momentum. This makes the onset of detachment sudden and conspicuous, and an accurate determination even of the higher-lying fine-structure thresholds becomes possible. The situation is significantly different for transition-metal negative ions, since they detach into a p-wave continuum. The onset of detachment is smooth and slow, and a determination of the actual threshold depends sensitively on a p-wave fit to the data above threshold. Series of cascaded p-wave thresholds are thus expected to be challenging and, to our knowledge, have not been studied previously.

It is the aim of the present paper to determine the feasibility of LPT spectroscopy for fine-structure measurements in transition-metal negative ions. Co^-, Ni^-, Rh^-, and Pd^- are chosen, as the fine structure of these systems has been previously investigated with LPES; a comparison of the two techniques is therefore possible. Early theoretical treatments of these four ions have employed semiempirical methods [14] such as horizontal analysis [15] or isoelectronic extrapolation [16] to obtain estimated EA values. *Ab initio* calculations of atomic EA's for systems with an open d shell are extremely challenging. Both electron correlations and relativistic effects play an important role [17]. To our knowledge, the errors associated with the EA calculations presented to date [18] are still significantly larger than the uncertainties of the respective experimental (LPES) values.

*Also with the Department of Engineering Physics, the Brockhouse Institute for Materials Research, and the Center for Electrophotonic Materials and Devices.

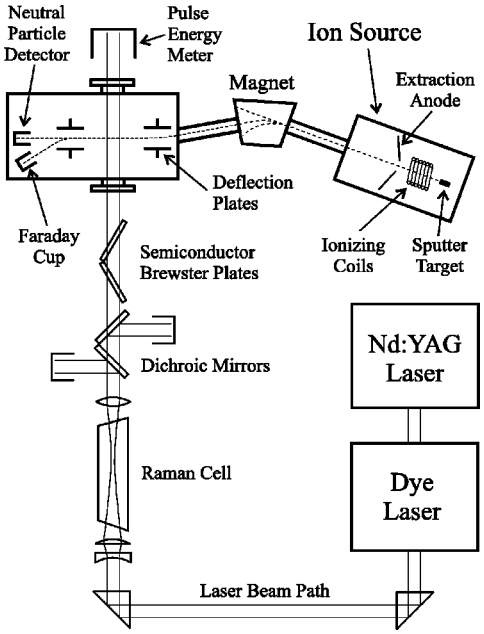

FIG. 1. Schematic diagram of the experimental setup. See text for details.

II. EXPERIMENTAL PROCEDURES

Figure 1 gives a schematic overview of the experimental apparatus that was used in the photodetachment studies described herein. The setup consists of a negative ion beam apparatus and an infrared laser source, arranged in a crossed-beam geometry. The beam apparatus is comprised of a cesium sputter source, a bending magnet, an interaction chamber, and detection electronics. The infrared laser source includes a Nd:YAG (neodymium:yttrium-aluminum-garnet) laser, a dye laser, and various optical components for wavelength conversion and filtering.

A. Ion-beam apparatus

The ion source is a home-built version of the high-intensity cesium sputter source developed by Middleton. The principle of operation of this type of negative ion source is described in detail elsewhere [19]. In brief, a continuous flow of cesium vapor is admitted into the evacuated (pressure $\leqslant 10^{-6}$ mbar) source chamber, where some of the cesium atoms condense on the cooled surface of the sputter target, while others are ionized by a heated tantalum coil. The target is negatively biased with respect to the ionizer such that the Cs^+ ions are accelerated and electrostatically focused onto the target. The cesium layer on the target reduces the effective work function of the sputter surface, and thereby greatly enhances the probability that an atom (or molecule) of the target material picks up an extra electron as it is sputtered off the surface. Once formed, the negative ions are accelerated through the ionizer and a subsequent extraction anode. Typical voltage settings in the experiments described here were 4 kV for the target bias and 10 kV for the extraction anode. The extracted ion beam is collimated with the aid of an electrostatic Einzel lens (not shown in Fig. 1), and then magnetically deflected through 30°. The magnet is operated at fields of $\leqslant 5.2$ kG, which enables a reasonable mass separation of the various ion-beam components ($\Delta M/M \approx 5\%$). Since cesium sputter sources operate with solid targets, the beam composition can indeed be manifold. In addition to atomic negative ions, the ions of dimers and trimers are often present, as well as the ions of oxides and various compounds which result from target impurities or from reactions of the target with the background gas of the source. In cases where the masses of atomic and molecular ions cannot be separated, the problem is often alleviated by the fact that most prolific molecular ions are too strongly bound to be photodetached by infrared light [1].

While the various source parameters are generally optimized to yield maximum beam currents of the ion species of interest, the present study also had to be concerned with the fractional population of different negative ion levels. The temperature of the sputter area gives rise to a Boltzmann population of the ionic energy levels, based on the assumption that the negative ions are able to thermalize before leaving the sputter surface. This temperature should depend on the energy and current of the sputter beam [19], but also on the size of the sputter area. The latter can be easily varied by moving the target back or forth. It was found that this has only a small effect on the total beam current but a significant effect on the population of excited ion levels. As expected, large excited level populations are obtained with the sputter target on focus, whereas the excited ion-beam currents are up to two orders of magnitude smaller with the target off focus. These tests and estimates based on previous photodetachment studies of Se^- and Te^- [20] indicate a range of 500–1500 K for the effective temperature of the sputter source.

Negative ions from a keV ion beam are easily detached in collisions with rest gas molecules, hence the background signal in a measurement of photodetachment events strongly depends on the collisional detachment rate. As this rate is proportional to the rest gas pressure, the photon-ion interaction is carried out in an ultrahigh vacuum (UHV) chamber at pressures of less than 10^{-8} mbar. The ion beam is fed into the interaction chamber through a differential pressure tube. Although the transmitted beam current is typically reduced by a factor of 2–5 the reduction in rest gas pressure of over two orders of magnitude still warrants a significant net improvement in the signal-to-background ratio. In the UHV chamber the ion beam is deflected through 10° by a pair of electrostatic deflection plates which removes any neutral particles from the beam, and brings the beam on axis with the detector. The ion beam then passes through the interaction region where it is crossed at 90° by a pulsed laser beam. A second pair of electrostatic deflection plates, located behind the interaction region, deflects the residual ion beam into a Faraday cup, while neutral particles that were produced in the photon-ion interaction remain unaffected and finally impinge on the open cathode of a discrete-dynode electron multiplier. The signal from the electron multiplier is passed through a fast preamplifier to minimize electronic noise, and is then fed into a gated integrator and boxcar averager. The gate is typically set to 50 ns, which provides a sufficiently large window for the detection of all photodetachment events resulting from a $\approx$8-ns laser pulse, and at the same time facilitates a substantial suppression of the collisional background count, down to ~ 0.1 events for a typical beam current of 100 nA. The data acquisition window is delayed by 1–2 μs relative to the laser pulse in order to accommodate the flight time of the photodetached neutral particles from the

interaction region to the detector. The time-of-flight difference between species of slightly different mass in fact enables a factor of 2 improvement in mass separation ($\approx 2\%$) if narrow gates and a tightly collimated (or focused) laser beam are used. In the experiments described here, the number of photodetachment events per pulse was usually larger than one, which is the reason the data acquisition was conducted via analog signal integration rather than digital pulse counting. Consequently, special care had to be taken that the electron multiplier would operate in a linear regime. The data are finally read from the boxcar averager by a personal computer for further processing.

B. Infrared laser source

The generation of tunable infrared light is based on a Nd:YAG laser, a Lumonics YM-800. The laser is operated with a *Q*-switched cavity, i.e., in a pulsed mode with a 10-Hz repetition rate. It is optimized to provide maximum output at 532 nm, the second harmonic of the fundamental YAG wavelength, with up to 400 mJ of energy in a ≈ 8 ns pulse. The pulse energy is stabilized against temperature drifts by purging the laser housing with cool nitrogen gas. The 532-nm laser pulse is used to pump a Lumonics HD-300 dye laser. This laser is operated with a 1800 lines/mm grating rather than the more common 2400 lines/mm grating in order to enable tunability over the 680–980 nm range. For this tuning range the spectral bandwidth of the laser ranges from 0.1 to 0.06 cm^{-1}. Accurate dye laser wavelength calibrations are routinely performed with a hollow cathode discharge lamp (made by Hamamatsu). Discharge lamps yield an optogalvanic effect, i.e., a measurable change in the discharge impedance whenever the laser wavelength is in resonance with certain atomic transitions of the filler gas [21]. In light of the near-infrared tuning range of our dye laser setup, argon is chosen as the filler gas as it offers many accurately known and optogalvanically active transitions ranging from 670 to 1150 nm [22].

The dye laser is optimized to achieve maximum pulse energies which results in a somewhat reduced quality of the spatial pulse profile. Typical pulse energies are 50 mJ at 700 nm, and 25 mJ at 950 nm. The associated peak powers of $\sim 10^7$ W are sufficient to achieve frequency conversion through the nonlinear optical properties of various media. In the present case, conversion of the dye laser pulses further into the infrared was tested with two different methods, difference frequency mixing in nonlinear optical crystals, and stimulated Raman scattering in a single-pass high-pressure hydrogen cell. The latter approach was finally chosen, as it provides a broader infrared tuning range with a simpler and less delicate optical setup. A 120-cm-long, 8-mm-diameter cell is used, filled with H_2 at a pressure of ≈ 22 bar. Good conversion of the dye laser pulse into first Stokes radiation (with quantum efficiencies of up to 40%) is achieved by focusing the ≈ 3-mm-diameter beam into the center of the cell. A Galilean telescope ($f_1 = -5$ cm, $f_2 = 10$ cm) with an effective focal length of ≈ 90 cm was utilized for this purpose. As stimulated Raman scattering is a coherent (although nonlinear) optical process, spatial, spectral, and temporal properties of the dye laser pulse are generally adopted by the first Stokes pulse. For a measured cell pressure of 22(1) bar

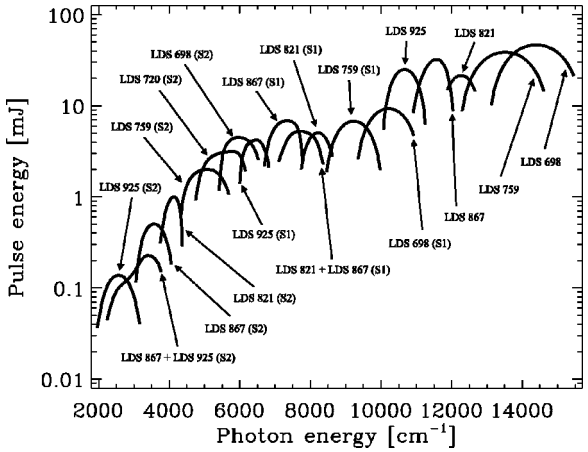

FIG. 2. Pulse energy curves for selected laser dyes and for the associated first and second Stokes conversions [indicated with the labels $(S1)$ and $(S2)$, respectively].

a Raman shift of 4155.187(5) cm^{-1} is expected, based on accurate studies of the pressure dependence of the fundamental Raman band in H_2 [23]. In addition, for first Stokes wavelengths shorter than 1150 nm the optogalvanic lamp could be used for a direct calibration of the Raman-shifted light. This yielded a shift of 4155.197(20) cm^{-1}, in excellent agreement with the literature value. The dye laser tuning range of 680–980 nm translates into a 950–1650-nm tuning range for the first Stokes light, although the use of different dyes is required for different regions of the tuning range. This is illustrated in Fig. 2, which shows pulse energy curves for the different dyes and their first and second Stokes conversions.

Conversion to second Stokes radiation becomes necessary whenever tunability beyond 1650 nm is required. Raman scattering of the first Stokes radiation, i.e., *sequential* stimulated Raman scattering would appear to be the most likely process for the generation of second Stokes radiation. However, the sequential scattering process has to compete against another nonlinear process, namely, parametric four-wave mixing, where the nonlinear susceptibility $\chi^{(3)}$ of the medium acts as the mixing parameter. Parametric four-wave mixing exhibits a somewhat different intensity and wavelength dependence than stimulated Raman scattering. As a result, it has been shown that Raman cells of sophisticated design are capable of suppressing the parametric process or at least some of its undesired properties. Such cells are Herriott-type multipass cells with refocusing geometry [24], or single-pass cells with capillary confinement of the focused laser beam [25]. Both these designs rely on a significant extension of the focused path length, which cannot be achieved with a simple single-pass cell. Hence, with the present setup second Stokes generation has to proceed via parametric four-wave mixing. The disadvantages of this process are an inevitable generation of various anti-Stokes orders, a lower theoretically achievable conversion efficiency, and the requirement of phase matching between the mixed waves. Despite the small dispersion of H_2 gas, the phase-matching requirement noticeably affects the spatial beam profiles; in contrast to the essentially Gaussian profiles of the dye laser and first Stokes beams, the second Stokes and anti-Stokes beam profiles are donut shaped, with an almost zero intensity at the center. Commensurate with its high order of

nonlinearity, the four-wave mixing process is found to be strongly dependent on the laser-pulse energy, the beam quality, and the focusing geometry, but only moderately dependent on the cell pressure, in agreement with other studies [26]. For the 3-mm-diameter dye laser beam used here, best results are obtained with a focal length around 120 cm and a focal position close to the exit window of the cell. The increased path length before the focus is believed to enhance the generation of first Stokes photons before the focus is reached, which then results in a more effective seeding of the four-wave mixing process [26]. For a dye laser tuning range of 680–980 nm, a second Stokes wavelength range of 1.6–5.2 μm is obtained, as shown in Fig. 2. Quantum conversion efficiencies of up to 25% are realized at shorter wavelengths, which is only a factor of 2 less than the efficiency achieved with multipass cells [24]. Although the conversion efficiency drops for longer wavelengths (down to 2% at 5 μm), it was still found to be sufficient in most of the photodetachment studies.

Further Raman conversion, i.e., the generation of third Stokes radiation is expected to be rather inefficient in a single-pass cell. In fact, we found no evidence of the presence of a third Stokes component in the Raman cell output, even for the most energetic pulses at 680 nm. Hence, the use of laser dyes that operate in the near infrared rather than the visible regime is of great advantage whenever a single-pass cell is utilized.

Various combinations of optical filters are employed to eliminate the unwanted wavelength components from the Raman cell output. In experiments that require the use of first Stokes radiation long-pass filters made from Schott glass are often sufficient to remove the dye laser and anti-Stokes wavelengths. Two rectangular filters are used, tilted in opposite directions to Brewster's angle. This minimizes reflection losses without introducing a lateral beam displacement. In cases where the second Stokes wavelength falls within the transmission range of the glass filter, no further filtering is deemed necessary as the presence of second Stokes radiation should not affect an experiment that uses the first Stokes beam. Whenever dye laser wavelengths beyond 800 nm or first Stokes radiation have to be suppressed, pairs of 45° dichroic mirrors are utilized to attenuate the unwanted beam components by $\approx$90%. The final filtering is then achieved with a Brewster-angle pair of semiconductor plates, made from either silicon or germanium. In all cases, a CaF_2 lens with an appropriate focal length is used to recollimate the Raman cell output such that the desired wavelength component would have a beam diameter of 3–5 mm. The infrared laser beam is finally transmitted via CaF_2 viewports through the interaction chamber, where it crosses the ion beam perpendicularly. The alignment of the crossing angle is crucial but had to be carried out only once (as described in Ref. [33]). This is a major advantage of using filters rather than dispersing prisms as wavelength-selective components; the laser-beam alignment becomes wavelength independent. A pyroelectric energy meter located behind the exit window is utilized to monitor the energy of the laser pulses. The energy meter as well as the entire infrared optics table are sealed off and purged with dry nitrogen gas, as infrared absorption-bands of atmospheric molecules such as CO_2 or H_2O would otherwise lead to a substantial laser-beam attenuation.

C. Data acquisition and analysis

The photodetachment cross section in the vicinity of a given threshold is recorded by performing a slow dye laser scan (20–30 min) over an appropriate wavelength range. The wavelength range is usually adjusted to provide sufficient information for both the region below and the region above threshold, which is particularly important in the case of *p*-wave detachment (see below). Depending on the ion-beam currents and infrared pulse energies available for a particular experiment, the signal-to-noise ratio of a single scan is often insufficient. The scan procedure is then repeated up to ten times, and individual scans are added together. The photodetachment data are finally normalized against ion-beam current and infrared pulse energy, which are recorded in all scans parallel to the neutral particle signal.

1. Threshold fit

After conversion of the scan range from dye laser wavelength to infrared photon energy, Wigner's *p*-wave threshold law [13] is fitted to the data. For any *p*-wave photodetachment channel the threshold law predicts a vanishing cross section for photon energies, ε, below the threshold energy, ε_0, whereas a cross section proportional to $(\varepsilon-\varepsilon_0)^{3/2}$ is predicted for $\varepsilon>\varepsilon_0$. However, in most of the cases investigated here other open photodetachment channels have to be taken into account. As long as the thresholds of these other channels are not too close to ε_0, their contributions to the total cross section in the vicinity of ε_0 are generally smooth and can be represented by a linear term. Therefore, the function that is fitted to the measured cross section is given by

$$\sigma=\begin{cases} a_0+a_1(\varepsilon-\varepsilon_0)+a_2(\varepsilon-\varepsilon_0)^{3/2} & \text{for} \quad \varepsilon>\varepsilon_0 \\ a_0+a_1(\varepsilon-\varepsilon_0) & \text{for} \quad \varepsilon\leqslant\varepsilon_0. \end{cases} \tag{1}$$

Two different methods of fitting this equation to the data are utilized. The first method employs a multiparameter gradient-expansion algorithm to perform a nonlinear least-squares fit. The fitting parameters a_0, a_1, a_2, and ε_0 are optimized simultaneously. In the second method a linear least-squares fit to the data below threshold is carried out first, in order to determine the photodetachment background. The fitted background is then subtracted from the data, which are subsequently linearized by exponentiating with 2/3. A linear least-squares fit finally provides the threshold value ε_0.

In previous studies of *p*-wave thresholds either one or the other method was used. For example, of the three independent LPT studies of the EA of platinum, the two more recent works [27,28] employed the first method while the earlier study [30] utilized the second method. The results of these studies differ by more than the respective error margins would suggest.

In comparison, the first fitting method constitutes a more rigorous approach, and also provides well-defined standard deviations for the fitted parameters. We found, however, that this method would also overcompensate for small systematic deviations from a *p*-wave curvature above threshold, through a small shift of the background line. This effect is due to the very slow increase of the *p*-wave cross section at threshold, and results in a small systematic shift of the fitted threshold

value. The second method, on the other hand, tends to undercompensate for systematic deviations in the above-threshold data. Hence the average of the two fitted threshold values is adopted as the final result. Its uncertainty is evaluated from the difference between the two fitted values and from the standard deviation obtained with the first method.

Although Eq. (1) is an exact description of the photodetachment cross section close to threshold, systematic deviations may occur at the high-energy end of a threshold scan. In this case, correction terms to the Wigner law would have to be taken into account [29]. However, previous studies of *p*-wave thresholds [30,10] have shown that the range of validity of the Wigner law is clearly larger for *p*-wave detachment than for *s*-wave detachment. Hence an inclusion of higher-order terms to the fitting function [Eq. (1)] is not deemed necessary here. Of more concern are possible systematic deviations from the Wigner threshold behavior due to a saturation of the detachment process, i.e., a depletion of the ionic levels by the intense laser pulse. The linearity of detachment signal versus pulse energy is therefore checked on a case to case basis. In some cases it is possible to optimize the signal-to-background ratio by adjusting the (average) pulse intensity such that the background channels are saturated while the threshold channel is still linear.

2. Threshold strength

The presence of more than one photodetachment channel is due to the existence of different electronic configurations, terms, or fine-structure levels in either the ion or the atom. For an ionic electron configuration with only one open shell (which is the *d* shell for most transition metal ions) the intensity for photodetachment from an ionic ^{2S+1}L term to an atomic $^{2S'+1}L'$ term is given by

$$I(LS,L'S') \propto n_l |\langle SL\{[S'L']l\rangle|^2 \times \sum_{l'=|l-1|}^{l+1} |\langle l\|\mu\|l'\rangle|^2. \quad (2)$$

Here n_l is the number of electrons in the open shell of the ion, $\langle SL\{[S'L']l\rangle$ is the fractional parentage coefficient for the decomposition of the ionic ^{2S+1}L term into an atomic $^{2S'+1}L'$ term and an l electron, and $\langle l\|\mu\|l'\rangle$ is the reduced matrix element of the electric dipole moment operator for the photodetachment of a bound l electron into the $\varepsilon l'$ continuum [31,32]. This $^{2S+1}L \rightarrow {}^{2S'+1}L'$ photodetachment transition is further composed of up to $(2S+1)(2S'+1)$ fine-structure transitions. In the case that the spin-orbit coupling of the electrons can be approximated by LS coupling, the relative intensity of a fine-structure transition $J \rightarrow J'$ is given by

$$I(J,J') \propto \sum_{j=|l-1/2|}^{l+1/2} (2j+1)(2J+1)(2J'+1) \times \begin{Bmatrix} S & L & J \\ \frac{1}{2} & l & j \\ S' & L' & J' \end{Bmatrix}^2 \exp\left(\frac{-E(J)}{kT}\right), \quad (3)$$

where l and j denote orbital and total angular momenta of the bound electron that is to be detached. (Note that the angular momentum l' of the detached electron, which determines the shape of the threshold, is not relevant here.) The properties of the $9J$ symbol in Eq. (3) determine the selection rules for photodetachment:

$$|\Delta S| \leqslant \tfrac{1}{2}, \quad |\Delta L| \leqslant l, \quad |\Delta J| \leqslant l+\tfrac{1}{2}. \quad (4)$$

For transition metals with both *s* and *d* valence electrons, l can be either 0 or 2. Typically, a large number of thresholds is allowed in the detachment of a *d* electron, but for *s*-electron detachment the number is clearly limited by the selection rules. The Boltzmann factor $\exp(-E(J)/kT)$ in Eq. (3) accounts for a thermal population of the different ionic energy levels, and must be included unless the level splittings are much smaller than kT, where T is the effective ion source temperature (see Sec. II A). T can be evaluated from Eq. (3) if it is possible to determine experimentally two fine-structure thresholds for a given ionic term, as the relative intensities are then given by the fitting parameter a_2 in Eq. (1). If the relative intensities of more than two thresholds are measured, a comparison with the theoretical predictions of Eq. (3) will indicate the validity of the LS coupling approximation for the particular ion.

3. Experimental uncertainties

The accuracy of a crossed-beam photodetachment experiment is ultimately limited by a number of factors such as the calibration uncertainty, the laser bandwidth, Doppler broadening, and possible Doppler shifts or thermal wavelength drifts. However, these various sources of error, which are described in detail in Ref. [33], typically give rise to an uncertainty of only ≈ 0.1 cm^{-1} or less. In the present study of cascaded *p*-wave thresholds, this contribution to the total experimental uncertainty is clearly dwarfed by the statistical uncertainty associated with the *p*-wave fit to the data, which is 1 cm^{-1} or more (see below).

III. RESULTS AND DISCUSSION

A. Nickel

Previous experimental studies of Ni^- in Refs. [34] and [35] have found the $J=\frac{5}{2}$ level of the $3d^9 4s^2\,{}^2D$ term to be the ionic ground state with binding energies of 1.157(10) and 1.15(15) eV, respectively. The authors of Ref. [34] also measured a value of 1470(100) cm^{-1} for the fine-structure splitting of the ^2D term. (Note that 1 eV = 8065.5410(24) cm^{-1} [36].) No indication was found for the existence of other bound ionic states. Due to this simple and well-established energy-level structure, Ni^- seemed to be a suitable candidate for a first attempt at photodetachment threshold spectroscopy with cascaded *p* waves. Unfortunately, the situation is complicated by the many low-lying energy levels of the atom, which arise from a near degeneracy between the $3d^9 4s$ and $3d^8 4s^2$ configurations. This can be seen in Fig. 3, which shows a schematic energy-level diagram for Ni^- and Ni. In addition to the ^3F term of the $3d^8 4s^2$ configuration, of which the $J=4$ level constitutes the atomic ground state, four other levels are present which belong to the ^3D and ^1D terms of the $3d^9 4s$ configuration. According to the selection

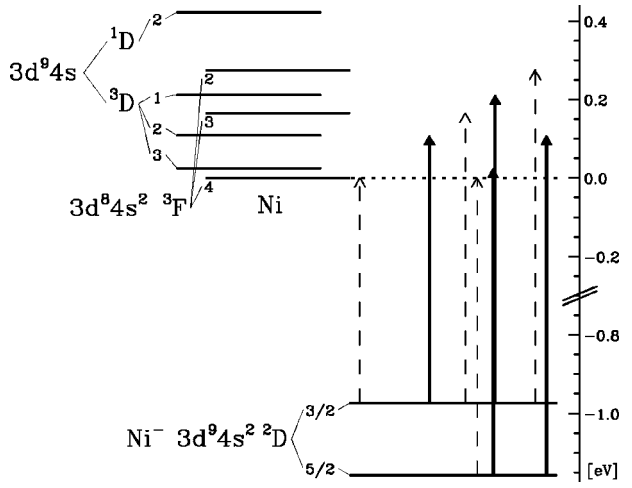

FIG. 3. Schematic energy-level diagram of Ni^- and Ni. Arrows indicate photodetachment thresholds expected to lie within the investigated photon energy range. Dashed or solid lines are used depending on whether a threshold is predicted to be weak or strong, respectively (see text). The horizontal spacing between arrows is proportional to the energy separation of the respective thresholds.

rules for photodetachment [Eq. (4)], the cross section of Ni^- should thus exhibit 12 thresholds within the near-infrared regime; the first eight are indicated by arrows in Fig. 3.

We have measured the photodetachment cross section of Ni^- over a photon energy range of 7500–10 400 cm^{-1}. Pulse energies ranged from 5 to 9 mJ (compare Fig. 2), and an ion-beam current of $\approx$250 nA was obtained from a sputter target made of high-purity nickel. Although the scan range covered eight of the 12 infrared thresholds, only two were observed. The part of the scan that displayed these two *p*-wave features is shown in Fig. 4. The result might seem surprising, but four of the possible eight thresholds were expected to be very weak, namely, those where a *d* electron is removed from the ionic configuration. Various LPES studies of transition-metal negative ions, including the investigation of Ni in Ref. [34], have indicated that photodetachment processes which involve the removal of a *d* electron are typically about an order of magnitude weaker than processes where an *s* electron is detached [32,34,37]. Hence, all of the

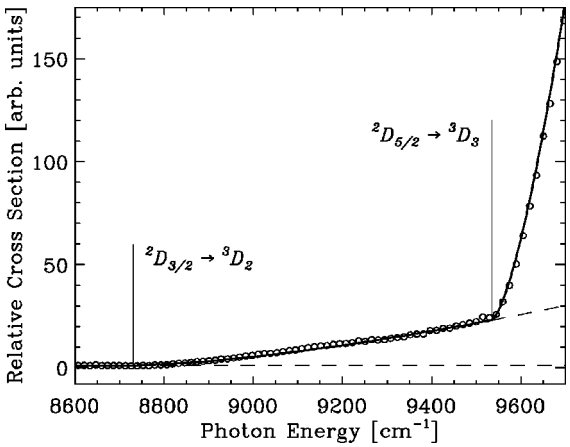

FIG. 4. Photodetachment cross section of Ni^-. Only the portion of the investigated photon energy range that exhibited threshold structures is shown.

TABLE I. Calculated intensities of Ni^- thresholds.

Threshold[a]	Relative intensity[b]		
	$T=\infty$	$T=650$ K	$T=1300$ K
$^2D_{3/2}\rightarrow{}^3D_2$	20.0	1.2	5.7
$^2D_{5/2}\rightarrow{}^3D_3$	46.7	75.9	68.8
$^2D_{3/2}\rightarrow{}^3D_1$	20.0	1.2	5.7
$^2D_{5/2}\rightarrow{}^3D_2$	13.3	21.7	19.7
$^2D_{3/2}\rightarrow{}^3F_4$	4.3	0.3	1.2
$^2D_{3/2}\rightarrow{}^3F_3$	16.7	1.0	4.8
$^2D_{5/2}\rightarrow{}^3F_4$	38.6	62.7	56.9
$^2D_{3/2}\rightarrow{}^3F_2$	19.0	1.2	5.5
$^2D_{5/2}\rightarrow{}^3F_3$	16.7	27.1	24.6
$^2D_{5/2}\rightarrow{}^3F_2$	4.8	7.7	7.0

[a]The thresholds within each group are ordered from low to high energies.

[b]The relative intensities within each group are given in percent of the total transition strength.

$^2D_J\rightarrow{}^3F_{J'}$ thresholds (except $J=\frac{3}{2}\rightarrow J'=4$, the threshold with the lowest energy, see below) are likely to be hidden in the detachment cross section resulting from the other thresholds. This suggests in particular that the $^2D_{5/2}\rightarrow{}^3D_3$ threshold (fifth arrow in Fig. 3) rather than the EA-defining $^2D_{5/2}\rightarrow{}^3F_4$ threshold (fourth arrow in Fig. 3) should be the first noticable threshold that originates from the ionic ground state. This $^2D_{5/2}\rightarrow{}^3D_3$ threshold can only be the second threshold seen in Fig. 4, as the first one occurs at a photon energy clearly smaller than the EA and must therefore result from the $^2D_{3/2}\rightarrow{}^3D_2$ transition. However, due to the near coincidence between the $^2D_{5/2}\rightarrow{}^3D_3$ and $^2D_{3/2}\rightarrow{}^3D_1$ thresholds, their relative intensities must be considered before an unambiguous assignment can be made. Table I comprises the relative intensities of the first ten infrared thresholds for a pure statistical population of the ionic levels ($T=\infty$), and for populations resulting from a ''cool'' ($T=650$ K) as well as a ''hot'' ($T=1300$ K) sputter source. According to these numbers, the contribution of the $^2D_{3/2}\rightarrow{}^3D_1$ transition to the second threshold feature in the detachment cross section is at a negligible level of $\approx$1–2% for a cool source while it is at a critical level of $\approx$10% for a hot source. Hence special care was taken that the source would operate at a relatively low temperature (as described in Sec. II A).

Both thresholds were finally scanned at a higher resolution to enable an accurate determination of the threshold energies. Values of 8728(3) and 9537.9(10) cm^{-1}, respectively, were obtained from a *p*-wave fit to the data. The scan over the region of the $^2D_{5/2}\rightarrow{}^3D_3$ threshold is shown in Fig. 5. A single *p* wave [Eq. (1)] fits the data well, indicating that the contribution of the $^2D_{3/2}\rightarrow{}^3D_1$ threshold is indeed negligible. The accuracy of the fit is mainly limited by the strong and sloped photodetachment background that originates from the $^2D_{3/2}\rightarrow{}^3D_2$ transition, and would have been worse for a higher ion source temperature. By subtracting the accurately known energies of the atomic levels involved [38] from the threshold values, the electron affinity of nickel is determined to be 9333.1(10) cm^{-1} [1.15716(12) eV], and a

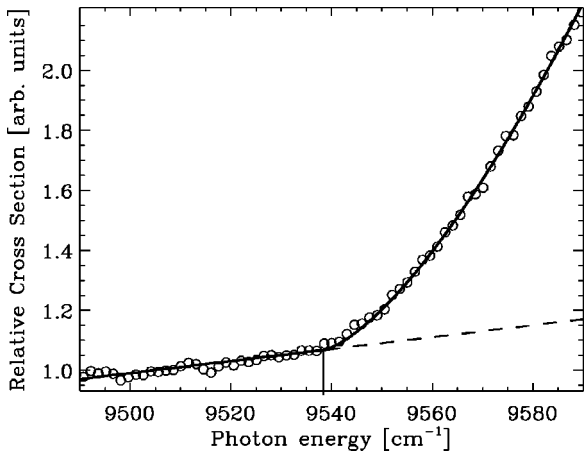

FIG. 5. Photodetachment cross section of Ni^- in the vicinity of the $^2D_{5/2}\rightarrow{}^3D_3$ threshold. The solid line indicates the result of a *p*-wave fit to the data.

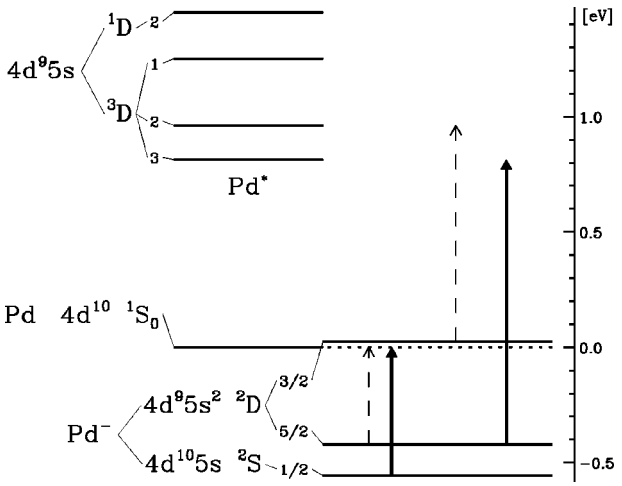

FIG. 6. Schematic energy-level diagram of Pd^- and Pd. The unobserved ionic $^2D_{3/2}$ level is probably unbound, as shown here. Solid arrows indicate observed photodetachment thresholds; dashed arrows represent thresholds too weak for observation with the present setup.

fine-structure splitting of 1485(3) cm^{-1} is obtained for the $Ni^-(^2D)$ term. These values are in excellent agreement with the results of Ref. [34], but constitute an improvement in accuracy of almost two orders of magnitude.

Since two thresholds were measured here, their relative intensities may be compared with the calculated values given in Table I in order to obtain the effective source temperature. A measured intensity ratio of 0.016(2) gives a temperature of 650(30) K, commensurate with the above considerations. More interestingly, the relative strengths of *s*-electron versus *d*-electron detachment can be evaluated from a comparison between the signal and the background of the (*s*-electron detaching) $^2D_{3/2}\rightarrow{}^3D_2$ threshold. The background must be due to the *d*-electron detaching $^2D_{3/2}\rightarrow{}^3F_4$ transition, $\approx$900 cm^{-1} above its threshold. (The threshold itself is too weak for a direct observation.) Under the assumption that the *p*-wave law is applicable 10% above threshold (as seems to be the case for the $^2D_{3/2}\rightarrow{}^3D_2$ threshold in Fig. 4) the actual threshold coefficient can be calculated, and an intensity ratio of 0.029(5) is obtained for the two thresholds. Normalizing this ratio with the relative threshold intensities (Table I) and with the appropriate coefficients from Eq. (2) finally yields a value of 22(6) for *s*-electron versus *d*-electron detachment of Ni^-. This number agrees with the range of 5–20 quoted in LPES studies [32,34,37], but the present value has the advantage of being a direct measure for the ratio of the reduced matrix elements $\langle s\|\mu\|p\rangle$ and $\langle d\|\mu\|p\rangle$ at *threshold* (where $\langle d\|\mu\|f\rangle$ is negligible), without the need to take energy dependencies (other than Wigner's law) into account [34].

It should be noted that the above derivations could be subject to a small systematic error as a result of the weak perturbation of the atomic $^3D_2$ level by the $^1D_2$ level. Corderman, Engelking, and Lineberger discussed this perturbation in detail, and showed that it may explain the increased strength of the $^2D_{5/2}\rightarrow{}^3D_2$ LPES peak that was observed in their study. If that is the case, the $^2D_{3/2}\rightarrow{}^3D_2$ transition should be proportionally weakened. However, a quantitative evaluation of this effect would have to rely on a comparison of $^2D_J\rightarrow{}^3D_{J'}$ and $^2D_J\rightarrow{}^1D_{J'}$ intensities, the latter of which cannot be derived from the present measurements of total cross sections.

B. Palladium

Despite the fact that palladium appears in the same column of the Periodic Table as nickel, the energy-level structure of both the atom and the negative ion is significantly different. The situation is illustrated in Fig. 6. In contrast to Ni, the order of the d^8s^2, d^9s, and d^{10} configurations is reversed for Pd: the ground state is given by $4d^{10}\,^1S_0$, and the ^3D and ^1D terms of the $4d^95s$ configuration give rise to the first four excited levels. The level structure of the ion was established by Feigerle *et al.* [37] in the only previous experimental study of this system. The analysis of their spectrum of LPES peaks revealed two final-state sequences, which indicated the existence of two bound energy levels in the ion. Based primarily on the detachment selection rules [Eq. (4)], these levels were identified as $4d^95s^2\,^2D_{5/2}$ and $4d^{10}5s\,^2S_{1/2}$, the latter being the ionic ground state. This is a striking contrast to the level structure of Ni^-, and constitutes the rather special case of a negative ion with two stable electronic configurations (albeit of the same parity). Feigerle *et al.* did not observe any LPES peaks that could have been assigned to the $J=\frac{3}{2}$ level of the ionic ^2D term. Based on an isoelectronic extrapolation, they estimated a binding energy of 6 ± 43 meV for this level, hence it is not established whether this level is weakly bound or slightly unbound with respect to the atomic ground state.

From the point of view of photodetachment threshold spectroscopy, the case of Pd^- is relatively straightforward. The first allowed threshold that can originate from the ionic ground state is $^2S_{1/2}\rightarrow{}^1S_0$, which also defines the EA of palladium. This threshold involves the detachment of an *s* electron, and is thus expected to be strong. Figure 7 shows the result of a photodetachment scan in the vicinity of this threshold. (A Pd^- current of 30 nA and pulse energies of $\approx$1.5 mJ were available in this experiment.) The *p*-wave fit to the data yields a threshold value of 4534.0(10) cm^{-1} [562.14(12) meV]. This value for the EA of Pd agrees with Feigerle *et al.*'s value of 558(8) meV, and marks a near 70-fold improvement in accuracy. The background signal seen in Fig. 7 is approximately three times larger than the purely

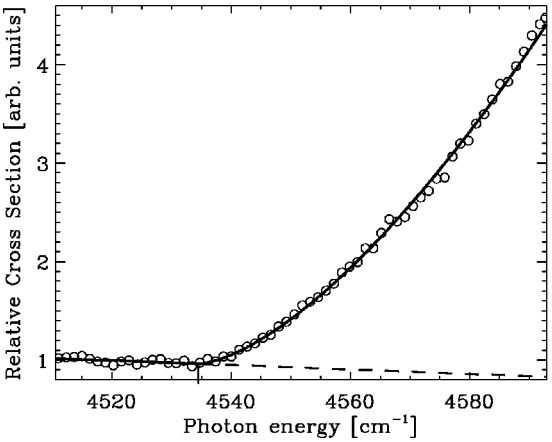

FIG. 7. Photodetachment cross section of Pd^- around the $^2S_{1/2}\rightarrow{}^1S_0$ threshold which defines the EA of Pd.

collisional background that is observed when the laser is blocked. It is attributed to the ''forbidden'' $4d^9 5s^2\,{}^2D_{5/2}\rightarrow 4d^{10}\,{}^1S_0$ photodetachment transition. This transition involves a two-electron process, and most likely draws its strength from a configuration interaction between the $^2D_{5/2}$ level and higher-lying resonance states of Pd^- [37]. It was also observed as a small peak in the LPES spectrum of Feigerle *et al.* The energy dependence of the cross section for such a forbidden detachment process is not known. It may very well display a slightly negative slope, as the background signal in Fig. 7 suggests.

The first allowed photodetachment transition involving the $^2D_{5/2}$ level of the ion is the *s*-electron detaching transition to the atomic $^3D_3$ level. Its threshold occurs at significantly higher photon energies than the $^2S_{1/2}\rightarrow{}^1S_0$ threshold discussed above. Therefore, the cross section in the vicinity of the $^2D_{5/2}\rightarrow{}^3D_3$ threshold will likely exhibit a substantial background due to the $^2S_{1/2}\rightarrow{}^1S_0$ transition. This is clearly seen in the photodetachment scan over that region, shown in Fig. 8. Although a threshold is undoubtedly present, its contribution to the total cross section amounts to only 20% for photon energies 200 cm^{-1} above threshold. An accurate determination of the threshold energy is nevertheless possible, primarily because the background is extremely flat. This circumstance might be due to a relatively flat cross section for the $^2S_{1/2}\rightarrow{}^1S_0$ transition over this particular photon energy range, and/or due to a saturation of that transition by the intense laser pulse. A threshold energy of 9971(4) cm^{-1} is obtained from the *p*-wave fit to the data. Subtracting the energy of the atomic $^3D_3$ level [39] finally results in a binding energy of 3407(4) cm^{-1} [422.4(5) meV] for the ionic $^2D_{5/2}$ level. This value compares favorably with the result of Feigerle *et al.*, 422(8) meV.

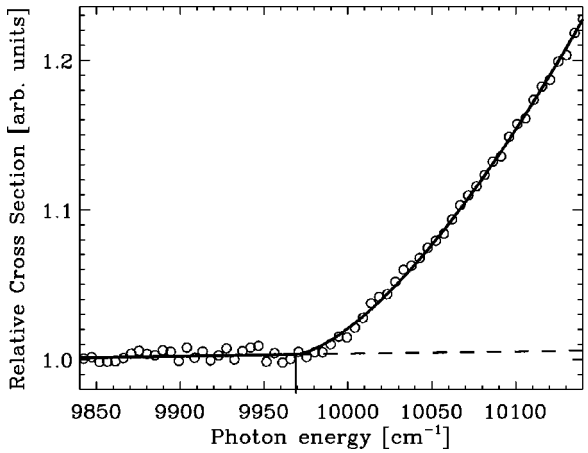

FIG. 8. Photodetachment cross section of Pd^- in the region of the $^2D_{5/2}\rightarrow{}^3D_3$ threshold, far above the EA-defining $^2S_{1/2}\rightarrow{}^1S_0$ threshold.

The relative detachment cross sections found in our threshold measurements unambiguously confirm the assignment of Pd^- energy levels made by Feigerle *et al.* The $4d^{10}5s\,{}^2S_{1/2}$ level must be the ionic ground state, with the $4d^9 5s^2\,{}^2D_{5/2}$ level lying 1127(4) cm^{-1} above it.

The single remaining question regarding the stable states of the ion is whether the $J=\frac{3}{2}$ level of the $4d^9 5s^2\,{}^2D$ term is also bound. If that were the case, the total cross section should in principle exhibit a threshold due to the detachment of thermal $^2D_{3/2}$ population into the $^3D_2$ level of the atom (which is the first allowed detachment channel). In practice, the thermal population would be rather small (even for a hot ion source), and its detachment into $^3D_2$ would be competing against the forbidden detachment into the atomic ground state and would also be subject to a strong background resulting from the $^2S_{1/2}\rightarrow{}^1S_0$ transition. Hence the lack of observation of the $^2D_{3/2}\rightarrow{}^3D_2$ threshold is not conclusive.

We therefore attempted to locate the $^2D_{3/2}$ level via the $^2D_{5/2}\rightarrow{}^2D_{3/2}$ magnetic dipole ($M1$) transition. It should occur at photon energies between 3100 and 3800 cm^{-1}, based on the isoelectronic extrapolation by Feigerle *et al.* [37]. The applicability of laser-driven $M1$ transitions to the study of negative ion fine structure has been demonstrated previously: first in an investigation of Ir^- and Pt^- [6], and recently in experiments on Te^- [40] and Sb^- [7]. The $4d^9 5s^2\,{}^2D$ term under investigation here is most similar to the $5d^9 6s^2\,{}^2D$ term that was studied in Pt^-, where the observed fine-structure $M1$ transition was in fact fairly strong. However, allowance has to be made for the fact that the fine-structure splitting in Pt^- is about three times larger than in Pd^-; hence pulse energies were about 20 times larger than the $\approx$0.5 mJ available in the present case. Furthermore, the Einstein *B* coefficient for the transition in Pd^- should be about a factor of 3 smaller than in Pt^-, as $M1$ rates roughly scale with the square of the nuclear charge. Also taking the difference in beam currents into account, resonance signals of less than one count per laser pulse were estimated for a tight focus of $\sim$50 μm. A tight focus was considered necessary, as for a bound (stable) $^2D_{3/2}$ level the detachment after the resonant transition had to proceed via a forbidden transition into the atomic ground state. An unbound $^2D_{3/2}$ level, on the other hand, would be metastable with respect to autodetachment, and is therefore expected to show up as a narrow resonance feature as well. We have searched for the Pd^- $M1$ transition in the photon energy range of 3050–3980 cm^{-1} with a scan rate of 200 laser pulses per cm^{-1} (15 pulses per laser bandwidth). No evidence of a resonance structure was found. Unfortunately, this result remains inconclusive as well. It is conceivable that the actual M1 transition strength is somewhat smaller than the above estimates suggest, perhaps too small for the sensitivity of the current setup. Further improvements of the experimental apparatus (or an entirely dif-

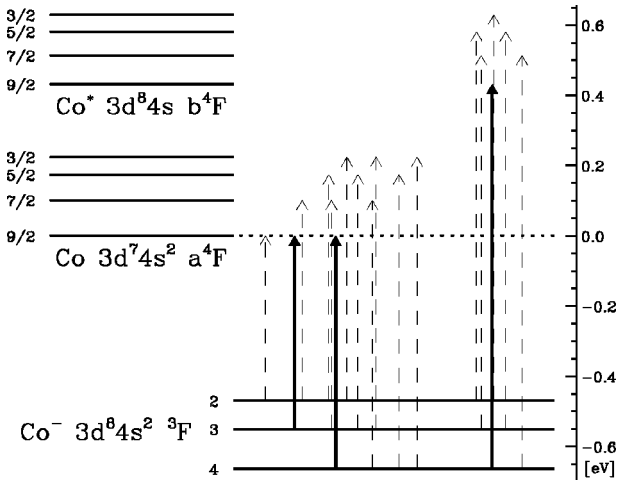

FIG. 9. Schematic energy-level diagram of Co^- and Co. The many infrared photodetachment thresholds of this system are indicated with arrows whose horizontal separation is proportional to the energy separation of the thresholds. The three thresholds that were measured here are shown with solid arrows.

ferent approach) seem therefore necessary for a determination of the $^2D_{3/2}$ binding energy.

C. Cobalt

An energy-level diagram for the negative ion of cobalt including the eight lowest-energy levels of the atom is shown in Fig. 9. The atomic levels are grouped into two ^4F terms (denoted as *a* and *b*) which belong to two different electron configurations, $3d^74s^2$ and $3d^84s$, respectively. Unlike the situation found in nickel, the average term energies are well separated here. The negative ion structure was first investigated in Ref. [34]. They identified the three fine-structure levels of the $3d^84s^2\,^3F$ term, and found no evidence for the existence of any other stable ionic states.

The major complication for a photodetachment threshold study of this system results from the fact that detachment to the first four atomic levels involves the removal of a *d* electron, and is thus expected to be weak. Strong channels of *s*-electron detachment, on the other hand, do not open up until photon energies are reached well above the threshold for ground-state detachment. Hence we expect that the corresponding (*s*-electron) threshold signals will have to compete against a substantial photodetachment background from the 12 open *d*-electron detachment channels.

The most promising thresholds for a LPT study were chosen on the basis of their calculated relative intensities. These intensities are listed in Table II, ordered by threshold energies. Again, values for a pure statistical level population ($T=\infty$), and for populations resulting from a ''cool'' ($T=650$ K) as well as ''hot'' ($T=1300$ K) sputter source were calculated. The EA of cobalt is defined by the $^3F_4 \rightarrow a^4F_{9/2}$ threshold, the sixth threshold in the sequence. Fortunately, the intensities of the first five thresholds are relatively small, particularly for $T=650$ K. Figure 10 shows the photodetachment signal that was recorded in the region of the sixth threshold, with the source operated at a low effective temperature, providing 350 nA of Co^-. In contrast to the thresholds studied in Ni^- and Pd^-, the photodetachment

TABLE II. Calculated intensities of Co^- thresholds.

Threshold[a]	Relative intensity[b]		
	$T=\infty$	$T=650$ K	$T=1300$ K
$^3F_2\rightarrow a^4F_{9/2}$	1.0	0.0	0.2
$^3F_3\rightarrow a^4F_{9/2}$	21.2	2.8	7.8
$^3F_2\rightarrow a^4F_{7/2}$	15.9	0.5	2.8
$^3F_2\rightarrow a^4F_{5/2}$	31.1	1.0	5.5
$^3F_3\rightarrow a^4F_{7/2}$	45.5	6.1	16.6
$^3F_4\rightarrow a^4F_{9/2}$	100.0	100.0	100.0
$^3F_2\rightarrow a^4F_{3/2}$	33.5	1.1	6.0
$^3F_3\rightarrow a^4F_{5/2}$	32.7	4.4	12.0
$^3F_4\rightarrow a^4F_{7/2}$	36.4	36.4	36.4
$^3F_3\rightarrow a^4F_{3/2}$	14.7	2.0	5.4
$^3F_4\rightarrow a^4F_{5/2}$	9.6	9.6	9.6
$^3F_4\rightarrow a^4F_{3/2}$	0.7	0.7	0.7
$^3F_2\rightarrow b^4F_{5/2}$	26.7	0.8	4.8
$^3F_3\rightarrow b^4F_{7/2}$	60.0	8.0	21.9
$^3F_4\rightarrow b^4F_{9/2}$	100.0	100.0	100.0
$^3F_2\rightarrow b^4F_{3/2}$	40.0	1.3	7.1
$^3F_3\rightarrow b^4F_{5/2}$	33.3	4.5	12.2
$^3F_4\rightarrow b^4F_{7/2}$	20.0	20.0	20.0

[a]Thresholds are ordered from low to high energies.
[b]Relative intensities are given in percent of the strongest transition within each group.

background here is strongly sloped, which is the limiting factor for the accuracy of the *p*-wave fit. A value of 5350(5) cm^{-1} [663.3(6) meV] was obtained, which compares very well with the EA value of 662(3) meV that was measured by Leopold and Lineberger via LPES [41]. The other three $^3F_4\rightarrow a^4F_J$, thresholds have smaller relative intensities than $^3F_4\rightarrow a^4F_{9/2}$ and can therefore not be expected to allow a more accurate EA measurement. The $^3F_4\rightarrow b^4F_{9/2}$ threshold, on the other hand, which is the first and also the strongest *s*-electron detaching threshold involving the ionic ground state, might be strong enough to allow at least a confirmation of the above EA value. A photon energy region of 8750–8950 cm^{-1} was scanned, and the threshold was

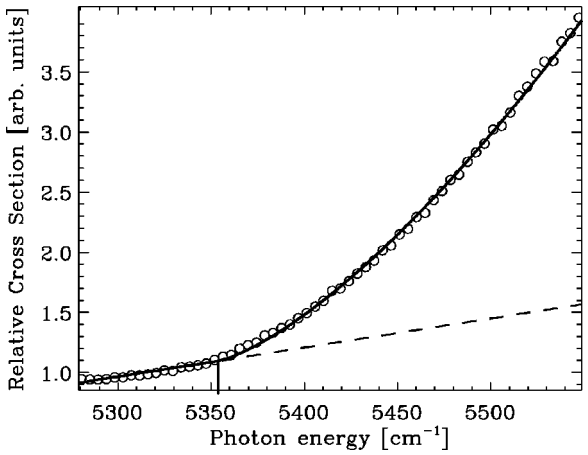

FIG. 10. Measured photodetachment cross section for the $^3F_4 \rightarrow a^4F_{9/2}$ threshold of Co^-, which defines the EA of cobalt.

found at 8845(15) cm^{-1}. As expected, the threshold was superimposed on a very large photodetachment background, which is the reason for the large uncertainty in the fitted value. Upon subtracting the $b^4F_{9/2}$ energy [38], an electron affinity of 5362(15) cm^{-1} [664.8(20) meV] is obtained, in agreement with the other values.

A determination of the negative ion fine structure seemed straightforward, as the two thresholds that are lowest in energy involve the two upper fine-structure levels. Unfortunately, the relative intensity of the first threshold, $^3F_2 \rightarrow a^4F_{9/2}$ is extremely small, only about 1% of the $^3F_4 \rightarrow a^4F_{9/2}$ intensity at $T=\infty$ (Table II). [This is a significant deviation from the 55% that one would expect on the basis of level degeneracies alone, without taking Eq. (3) into account.] The detachment signals measured for this channel were in fact so small that a determination of the threshold became impossible. The $^3F_3 \rightarrow a^4F_{9/2}$ threshold, on the other hand, could be measured, as its relative intensity is clearly higher (21% at $T=\infty$). Signal levels were still small, and even after several hours of scanning the signal-to-noise ratio remained poor. A threshold value of 4475(15) cm^{-1} was measured, which translates into a $J=4$–3 fine-structure splitting of 875(15) cm^{-1}, in good agreement with Corderman, Engelking, and Lineberger's value of 910(50) cm^{-1} [34]. A further investigation of the ionic fine structure via other (including *s*-electron detaching) thresholds was not attempted, as the calculated threshold intensities indicated rather unfavorable signal-to-background ratios.

D. Rhodium

Rhodium is found in the same group of the Periodic Table as cobalt and also forms a stable negative ion only in the $(n-1)d^8ns^2$ electron configuration. This was established in a LPES measurement by Feigerle *et al.* [37], which is, to our knowledge, the only previous study of this system. That investigation determined a binding energy of 1.138(8) eV for the $(4d^85s^2)\ ^3F_4$ ionic ground state and $J=3-4$ and 2–3 fine-structure splittings of 2370(65) and 1000(65) cm^{-1}, respectively. These values have been used in the schematic energy-level diagram of Rh^- and Rh shown in Fig. 11. In comparison to cobalt, the situation is simplified here due to the different order of energy levels in the atom. The $(n-1)d^7ns^2\,^4F$ term, which gave rise to the manifold of weak Co^- thresholds, is located above the $4d^85s\,^3F$ term of Rh. Hence the low-energy region of the photodetachment cross section of Rh^- is characterized by only six (*s*-electron detaching) thresholds.

An initial investigation of the cross section in the vicinity of the EA-defining $^3F_4 \rightarrow {}^4F_{9/2}$ threshold revealed a clean *p*-wave threshold, but the signal-to-noise ratio was poor due to a surprisingly low ion-beam current. The beam current in the UHV interaction chamber was only 6 nA. Based on a comparison of the Co^-, Ni^-, and Pd^- currents obtained here with the ion currents reported by Middleton [42], a substantially higher Rh^- current of $\sim$50 nA was expected. We are unable to provide a satisfactory explanation for this poor performance of the ion source, which was also observed for the transition metals chromium and molybdenum [43].

Nevertheless, after scanning the $^3F_4 \rightarrow a^4F_{9/2}$ threshold for several hours, a *p*-wave fit to the final data yielded a

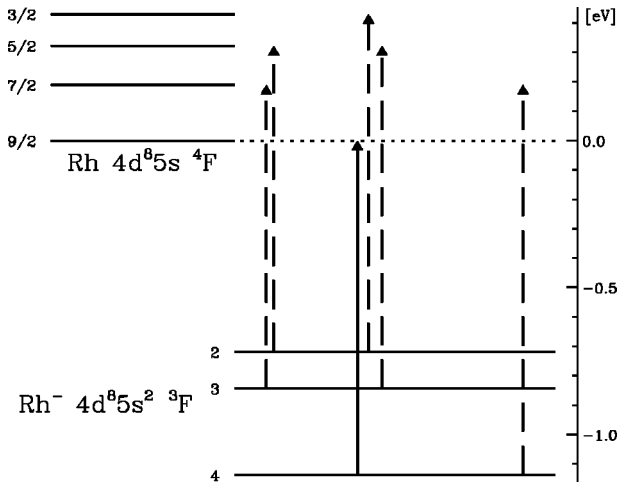

FIG. 11. Schematic energy-level diagram of Rh^- and Rh. Arrows indicate the first six detachment thresholds of which only the EA-defining $^3F_4 \rightarrow {}^4F_{9/2}$ threshold was measured (solid arrow).

threshold energy of 9218.0(15) cm^{-1} [1.142 89(20) eV]. This result for the EA of rhodium is in good agreement with the value of 1.138(8) eV found by Feigerle *et al.* [37], but constitutes a 40-fold improvement in accuracy. In light of the small ion-beam current, special care was taken in optimizing the position of the sputter cathode for a high effective temperature. Still, the detachment signal measured below the EA threshold remained small. This signal must be attributed to detachment from the two upper fine-structure levels. It was simply too small for an accurate determination of the actual thresholds, namely, $^3F_3 \rightarrow a^4F_{7/2}$ and $^3F_2 \rightarrow a^4F_{5/2}$, which are expected at photon energies of approximately 8330 and 8400 cm^{-1}, respectively. Provided that better Rh^- currents can be obtained, it should at least be possible to measure the first of these two thresholds. For a hot ion source this threshold would appear with $\approx$5% of the intensity of the EA threshold, which is comparable to the situation found for Ni^- (Sec. III A). The second of the two thresholds has a relative intensity of only 0.5%, and will probably always be obscured by the detachment signal of the first threshold.

E. Summary and outlook

Table III summarizes the results of our infrared LPT studies of the Co^-, Ni^-, Rh^-, and Pd^- negative ions, and also gives the values obtained in previous LPES studies for comparison. As can be seen, improvements in accuracy of up to two orders of magnitude were realized for both electron affinities and ionic fine-structure splittings. Infrared LPT spectroscopy has thus proven to be a valuable tool for the study of negative ions that exhibit multiple *p*-wave thresholds. However, the experiments have also indicated some of the limitations of the technique. The limitations mostly result from the fact that the present experimental setup utilized neutral particle detection to monitor the photodetachment process. Neutral atoms produced via different photodetachment channels cannot be separated, i.e., only the total cross section for photodetachment is measured. Consecutive channels thus appear as a ''cascade'' of thresholds in the neutral particle signal of an LPT study, as opposed to the series of

TABLE III. Summary of measured binding energies and fine-structure splittings.

		Binding energy (meV)		
Ion	Level	This work	Previous works	Ref.
Co^-	$^3F_4$	663.3(6)	662(3)	[41]
Ni^-	$^2D_{5/2}$	1157.16(12)	1157(10)	[34]
Rh^-	$^3F_4$	1142.89(20)	1138(8)	[37]
Pd^-	$^2S_{1/2}$	562.14(12)	558(8)	[37]
	$^2D_{5/2}$	422.4(5)	422(8)	[37]
		Fine-structure splitting (cm^{-1})		
Ion	Levels	This work	Previous works	Ref.
Co^-	$^3F_4-^3F_3$	875(15)	910(50)	[34]
	$^3F_3-^3F_2$	[a]	650(50)	[34]
Ni^-	$^2D_{5/2}-^2D_{3/2}$	1485(3)	1470(100)	[34]
Rh^-	$^3F_4-^3F_3$	[a]	2370(65)	[37]
	$^3F_3-^3F_2$	[a]	1000(65)	[37]

[a]Could not be measured in the present study.

individual peaks observed in the electron spectrum of a LPES measurement. This is not necessarily a limitation in the case of *s*-wave detachment, but, for *p*-wave channels, the detachment signal at threshold is notoriously small. The present study has shown that only the two or three strongest thresholds within a sequence of cascaded *p*-wave thresholds can be measured with an accuracy that is clearly superior to accuracies achieved with LPES. In cases such as Co^-, where a large number of thresholds is present, most thresholds cannot be resolved, as their strength relative to the photodetachment background is too small. In such cases an unambiguous interpretation of the LPT spectrum has to rely on previous LPES results in addition to calculated threshold strengths. Fortunately, the EA's of most of the remaining transition-metal negative ions that could be studied in LPT experiments have been previously measured via LPES, so the average term energies are known.

The limitations described above could be removed by implementing techniques for a channel-selective detection of the photodetachment products. An approach which seems particularly promising was used in the LPT study of alkali negative ions with visible light [9]. There the photodetached electrons were monitored through an electron spectometer as the laser was tuned. Electrons resulting from different detachment channels then appear as separated peaks in the spectrum, and the dependency of a particular peak on the photon energy is directly proportional to the partial cross section of the respective detachment channel. Hence a combination of this detection scheme with the infrared LPT techniques demonstrated here should in principle allow a resolution of dense threshold manifolds as found in Co^-. In practice, ion-beam energies higher than those used here would probably be required in order to provide threshold electrons with sufficient energy for detection. If necessary, the signal-to-noise ratio could always be improved by using an interaction region with collinear rather than crossed laser and ion beams. Resonant ionization spectroscopy (RIS) constitutes an alternative approach for state-selective detection. In recent years, this technique has been very successfully applied to the study of alkaline-earth negative ions [3]. The excellent signal-to-noise ratio achievable with RIS enables the detection of even the weakest detachment channels. On the other hand, the atomic energy-level structure of the element under investigation must provide for a practical resonant ionization scheme, which might not be the case for some transition metals.

A very different approach to the study of the fine structure of transition-metal negative ions could involve two-photon rather than single-photon threshold spectroscopy. The observation of two-photon detachment thresholds has been reported for three main group negative ions, namely, H^- [44], Cl^- [45], and Si^- [33]. This detachment scheme is particularly interesting for transition-metal negative ions, as their two-photon thresholds follow the Wigner *s*-wave law with its characteristic sharp onset. Cascades of even closely spaced *s*-wave thresholds have proven to be an accurate measure of ionic fine structure [11]. The threshold shifts that are inevitable with the high laser intensities necessary for the two-photon process would likely be the same for all fine-structure thresholds, and thus the splitting would remain unchanged.

Both LPT and LPES studies depend on an initial population of the ionic levels to be investigated. Hence, for a ''thermal'' ion source, bound states that lie more than ~ 0.5 eV above the ionic ground state typically remain undetected. A study of such high-lying bound ionic states would have to employ a ''nonthermal'' ion source (e.g., a charge-exchange chamber) or resonant multiphoton schemes in the detachment process. Resonant multiphoton detachment from atomic negative ions was only recently demonstrated. These experiments located the excited state under investigation via a laser-driven two-photon electric-dipole [5] or single-photon magnetic-dipole [6] transition from the (same parity) ionic ground state. (There is yet no experimental evidence that any atomic negative ion would exist in two stable configurations of opposite parity [46].) Although the present study of the Pd^- ion was unsuccessful in the attempt to drive the ^2D fine-structure transition, we still believe that multiphoton techniques are very promising for further investigations of transition-metal ions. In several systems an accurate fine-structure determination seems possible via a 2(Raman)+1 photon detachment scheme, as it was used in a study of Se^- and Te^- [20]. In addition, the near degeneracy of $(n-1)d^m$, $(n-1)d^{m-1}ns$, and $(n-1)d^{m-2}ns^2$ configurations found in most transition-metal atoms suggests that the respective ions may exist in more than one stable electron configuration. However, Pd^- is the only experimentally proven case thus far. A single-photon transition between two such configurations will be of electric quadrupole nature and therefore extremely weak, but a two-photon transition might be sufficiently strong in some cases.

IV. CONCLUSION

This paper has described photodetachment threshold experiments on transition-metal negative ions possessing more than one stable state. A case study of the Co^-, Ni^-, Rh^-, and Pd^- ions has resulted in significantly improved values for the electron affinities of these elements, and in most cases has also provided accurate measurements of ionic fine-

structure splittings. The experimental approach was based on a tunable infrared laser source, and is believed to be applicable to most of the remaining transition-metal negative ions. The limitations of the technique, as well as possible improvements and alternative detachment schemes, have been discussed.

ACKNOWLEDGMENTS

We gratefully acknowledge the Natural Science and Engineering Research Council of Canada (NSERC) for support of this work. We are also thankful to J. D. Garrett for manufacturing the various sputter cathodes.

[1] D. R. Bates, Adv. At., Mol., Opt. Phys. **27**, 1 (1991); T. Andersen, Phys. Scr. **T34**, 234 (1991).
[2] S. J. Buckmann and C. W. Clark, Rev. Mod. Phys. **66**, 539 (1994).
[3] T. Andersen, H. H. Andersen, P. Balling, P. Kristensen, and V. V. Petrunin, J. Phys. B **30**, 3317 (1997).
[4] C. Blondel, Phys. Scr. **T58**, 31 (1995).
[5] P. Kristensen, H. Stapelfeldt, P. Balling, T. Andersen, and H. K. Haugen, Phys. Rev. Lett. **71**, 3435 (1993).
[6] J. Thøgersen, M. Scheer, L. D. Steele, H. K. Haugen, and W. P. Wijesundera, Phys. Rev. Lett. **76**, 2870 (1996).
[7] M. Scheer, H. K. Haugen, and D. R. Beck, Phys. Rev. Lett. **79**, 4104 (1997).
[8] H. Hotop and W. C. Lineberger, J. Phys. Chem. Ref. Data **14**, 731 (1985).
[9] J. Dellwo, Y. Liu, D. J. Pegg, and G. D. Alton, Phys. Rev. A **45**, 1544 (1992).
[10] D. Feldmann, Z. Phys. A **277**, 19 (1976).
[11] M. Scheer, R. C. Bilodeau, and H. K. Haugen, Phys. Rev. Lett. **80**, 2562 (1998).
[12] M. Scheer, R. C. Bilodeau, J. Thøgersen, and H. K. Haugen, Phys. Rev. A **57**, R1493 (1998).
[13] E. P. Wigner, Phys. Rev. **73**, 1002 (1948).
[14] H. Hotop and W. C. Lineberger, J. Phys. Chem. Ref. Data **4**, 539 (1975).
[15] R. J. Zollweg, J. Chem. Phys. **50**, 4251 (1969).
[16] O. P. Charkin and M. E. Dyatkina, Zh. Strukt. Khim. **6**, 422 (1965) [J. Struct. Chem. (USSR) **6**, 397 (1965)].
[17] J. M. Garcia de la Vega, Phys. Rev. A **51**, 2616 (1995).
[18] E. Clementi, Phys. Rev. **135**, A980 (1964); Y. Guo and M. A. Whitehead, Phys. Rev. A **38**, 3166 (1988); J. M. Garcia de la Vega, J. Phys. B **27**, L447 (1994).
[19] R. Middleton, Nucl. Instrum. Methods Phys. Res. **214**, 139 (1983).
[20] J. Thøgersen *et al.*, Phys. Rev. A **53**, 3023 (1996).
[21] J. R. Nestor, Appl. Opt. **21**, 4154 (1982).
[22] L. Minnhagen, J. Opt. Soc. Am. **63**, 1185 (1973).
[23] W. K. Bischel and M. J. Dyer, Phys. Rev. A **33**, 3113 (1986); E. C. Looi, J. C. Stryland, and H. L. Welsh, Can. J. Phys. **56**, 1102 (1978), and references therein.
[24] P. Rabinowitz, B. N. Perry, and N. Levinos, IEEE J. Quantum Electron. **22**, 797 (1986).
[25] W. Heuer and H. Zacharias, IEEE J. Quantum Electron. **24**, 2087 (1988).
[26] H. Bryant, K. Sentrayan, and V. Kushawaha, Spectrosc. Lett. **25**, 1387 (1992).
[27] J. Thøgersen, L. D. Steele, M. Scheer, C. A. Brodie, and H. K. Haugen, J. Phys. B **29**, 1323 (1996).
[28] N. D. Gibson, B. J. Davies, and D. J. Larson, J. Chem. Phys. **98**, 5104 (1992).
[29] J. W. Farley, Phys. Rev. A **40**, 6286 (1989); T. F. O'Malley, Phys. Rev. **137**, A1668 (1964).
[30] H. Hotop and W. C. Lineberger, J. Chem. Phys. **58**, 2379 (1973).
[31] P. A. Cox, in *Structure and Bonding*, edited by J. D. Dunitz *et al.* (Springer-Verlag, Berlin, 1975), Vol. 24, pp. 59–81.
[32] P. C. Engelking and W. C. Lineberger, Phys. Rev. A **19**, 149 (1979).
[33] M. Scheer, R. C. Bilodeau, C. A. Brodie, and H. K. Haugen, Phys. Rev. A (to be published).
[34] R. R. Corderman, P. C. Engelking, and W. C. Lineberger, J. Chem. Phys. **70**, 4474 (1979).
[35] D. Feldmann, R. Rackwitz, E. Heinicke, and H. J. Kaiser, Z. Phys. A **282**, 143 (1977).
[36] E. R. Cohen and B. N. Taylor, Rev. Mod. Phys. **59**, 1121 (1987).
[37] C. S. Feigerle, R. R. Corderman, S. V. Bobashev, and W. C. Lineberger, J. Chem. Phys. **74**, 1580 (1981).
[38] J. R. Fuhr, W. C. Martin, A. Musgrove, J. Sugar, and W. L. Wiese, http//;physics.nist.gov.
[39] *Atomic Energy Levels*, edited by C. E. Moore, Natl. Stand. Ref. Data Ser., No. 35 (U.S. GPO, Washington, DC, 1971).
[40] M. Scheer, R. C. Bilodeau, and H. K. Haugen, J. Phys. B **31**, L11 (1998).
[41] D. G. Leopold and W. C. Lineberger, J. Chem. Phys. **85**, 51 (1986).
[42] R. Middleton (unpublished).
[43] R. C. Bilodeau, M. Scheer, and H. K. Haugen, J. Phys. B (to be published).
[44] C. Y. Tang *et al.*, Phys. Rev. Lett. **66**, 3124 (1991).
[45] R. Trainham, G. D. Fletcher, and D. J. Larson, J. Phys. B **20**, L777 (1987).
[46] M. Scheer *et al.*, Phys. Rev. Lett. **80**, 684 (1998).